2014 IEEE International Conference on Robotics & Automation (ICRA)
Hong Kong Convention and Exhibition Center
May 31 - June 7, 2014. Hong Kong, China

Toward Parallel Continuum Manipulators

Caroline E. Bryson, and D. Caleb Rucker *Member, IEEE*

***Abstract*— In this paper, we investigate continuum manipulators that are analogous to conventional rigid-link parallel robot designs. These "parallel continuum manipulators" have the potential to inherit some of the compactness and compliance of continuum robots while retaining some of the precision, stability, and strength of rigid-link parallel robots, yet they represent a relatively unexplored area of the broad manipulator design space. We describe the construction of a prototype manipulator structure with six compliant legs connected in a parallel pattern similar to that of a Stewart-Gough platform. We formulate the static forward and inverse kinematics problems for such manipulators as the solution to multiple Cosserat-rod models with coupled boundary conditions, and we test the accuracy of this approach in a set of experiments, including the prediction of leg buckling. An inverse kinematics simulation of slices through the 6 degree-of-freedom (DOF) workspace illustrates the kinematic mapping, range of motion, and force required for actuation, which sheds light on the potential advantages and tradeoffs that parallel continuum manipulators may bring. Potential applications include miniature wrists and arms for endoscopic medical procedures, and lightweight compliant arms for safe interaction with humans.**

I. INTRODUCTION

Continuum manipulators have historically been considered serial devices, perhaps because they typically have a long slender form, and the dominant geometric modeling paradigm is constant curvature arc segments tangentially connected in series, as reviewed in [1]. However, as some researchers have noted, many continuum designs also contain aspects resembling parallel architectures. For example, multiple entities are often constrained and connected in parallel within a single arc segment to achieve 2-DOF bending actuation (e.g. pneumatic muscles [2], multi-backbone designs [3], multiple embedded tendons [4]–[6], and concentric precurved tubes [7], [8]). Thus, the majority of existing continuum robots would most accurately be categorized as either serial or hybrid manipulators. In this paper, we consider continuum robot designs that are directly analogous to conventional rigid-link parallel robots. These "parallel continuum manipulators" constitute a relatively unexplored quadrant of the broad manipulator design space shown in Figure 1.

The continuum robots most closely related to this concept are snake-like multi-backbone designs, such as [3]. These employ a series of several bending segments, each of which is actuated by the translation of three parallel backbone rods. These parallel rods are constrained by several intermediate spacer disks such that the robot shape can be described by a series of frames along a single backbone curve. Use of a 3-DOF parallel continuum wrist design was also shown by Simaan in [9]. Similarly, the the bionic tripod manipulator from the German company Festo uses four flexible actuation rods connected in parallel through an intermediate constraint platform [10].

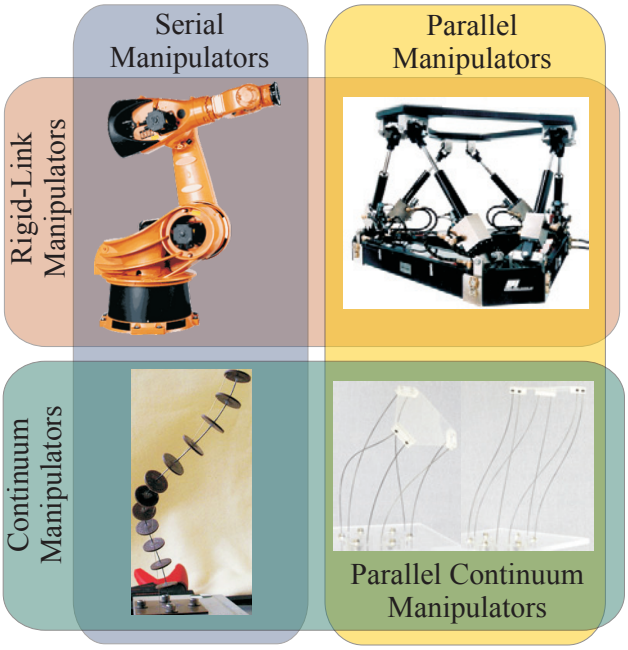

Fig. 1. The landscape of manipulator structural types contains the broad categories of *serial* and *parallel* robots. Continuum robots have a slender elastic structure and are typically considered serial robots. We seek to investigate the relatively unexplored fourth quadrant between parallel and continuum robots.

In the parallel robot research literature, flexible parallel robots have been studied extensively, as detailed in [11]. Past work has studied planar parallel robots with compliant links [12]–[15], as well as flexible Stewart platforms [16], [17], and the typical concern is with small link deformations that occur due to external or inertial loads. Parallel robots with flexure joints have also been studied, including and flexure-jointed 6 DOF platforms [18]–[21], high-precision robots [22], [23], mechanisms for micro/nano-manipulation [24], [25], and 3 DOF translation platforms [26]. In medical robotics, parallel robots with elastic actuation and flexure joints have been developed for rehabilitation [27], [28], and capsule endoscopy [29]. Parallel continuum robots differ in that they exhibit large, nonlinear, link deflections by design,

C. E. Bryson and D. C. Rucker are with the University of Tennessee, Knoxville, TN 37996, USA (e-mail: cbryson5@utk.edu, caleb.rucker@utk.edu).

and bending is distributed along the entire link rather than lumped at a specific a point. A patent application [30] by Zhu, et al. describes the essential concept of a parallel continuum manipulator from this perspective.

Thus, parallel continuum manipulators build on several ideas presented in prior work, yet the concept has not been fully explored with respect to modeling, analysis, design, and control. In the following sections, we present some progress toward these goals by describing the design and construction of a prototype parallel continuum structure and deriving a general kinematic modeling approach based on Cosserat rod theory. Then, we investigate the kinematic capabilities of our prototype and experimentally evaluate model accuracy.

A. Concept and Motivation

The basic design paradigm of a parallel continuum robot is illustrated in Figure 2. The distal ends of multiple compliant legs are connected in some pattern to an end effector platform, and the base of each leg is independently translated by an actuator at its proximal end. There may also be some additional constraints on the relative positions of the rods at a certain point (e.g. linear bearings where the rods pass through a base platform). One can conceive of several different variations of parallel continuum robot designs. As with rigid-link parallel manipulators, kinematic behavior is defined by the number of legs and the types of actuation and constraints at each end, which could vary from spherical to clamped joints (our prototype manipulator in Figure 3 uses clamped joints). The elastic legs themselves could be initially straight or have generally precurved stress free states, which could alter the kinematic properties of the device. Using tubes for the legs would allow wires or other infrastructure to be passed through their hollow center channels to the distal platform in order to actuate a gripper or other end effector. Using tubes would also enable hybrid "stacked" designs to be constructed (similar to multi-segment, snake-like designs, except with more degrees of freedom per segment) where the legs of a secondary parallel continuum mechanism extend out the ends the tubes through the distal platform of the primary mechanism.

In comparison to serial continuum robots, parallel continuum designs are likely to have higher payload capacity and accuracy/repeatability. Compared to rigid-link parallel manipulators, they may exhibit greater compliance, larger workspace, and easier miniaturization to the the scale of a few millimeters in diameter or smaller. Their inherent mechanical compliance and low mass due to off-loading of the actuators can provide an important safety feature wherever parallel robots need to interact with humans. In the field of endoscopic robotic surgery, parallel continuum manipulators have the potential to provide precise, multi-DOF motion in a simple, compact, and short mechanism at the tip of an endoscope. This capability may be useful for manipulating objects within highly confined spaces where a long slender body would be constrained by anatomical structures. In these cases, access to the site could be gained through flexible endoscopy, and then a parallel continuum device could provide fine, multi-DOF motion at the tip location (actuated by rods passing through hollow channels).

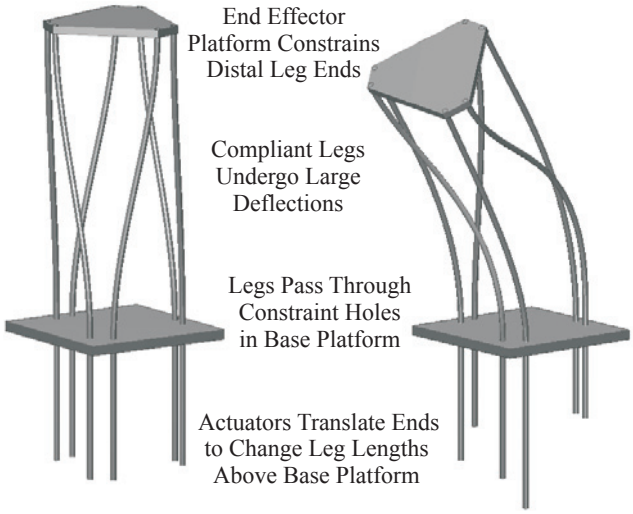

Fig. 2. The parallel continuum design paradigm utilizes the translation of slender rods between constrained points to create large deflections in each of the flexible legs.

II. Prototype Design and Construction

In this section we describe the construction of a parallel continuum manipulator prototype structure designed to show proof-of-concept and study parallel continuum robot behavior. The prototype has six compliant legs connected in a similar arrangement to the legs of a 6-DOF rigid-link Stewart-Gough platform, and each leg can be manually actuated. The legs consist of 1.3 mm diameter spring steel music wire (ASTM A228) with an estimated Young's modulus of 207 GPa and Poisson's ratio of 0.305. As shown in Figure 3, these rods are connected to an end-effector plate of clear $1/16$ inch acrylic via $3/8$ inch OD shaft collars constrained in channels within small blocks attached to the plate. The rods are routed through holes in the base plate, and the proximal ends are connected to linear slide carriages in the same fashion. The carriages translate along T-slotted aluminum rails (80/20® Inc.) that are bolted in a hexagonal pattern to the base plate. The linear slide carriages can be manually repositioned and locked in place with a brake so that the length of each rod between the base plate and the end plate can be actuated independently.

The connection locations of the 6 flexible legs are arranged in a conventional radial hexapod pattern of 3 pairs of rods spaced 120° apart at a radius of 87 mm. As depicted by the numbers in Figure 3, the proximal holes for rods 1 and 2 are paired together (with a total separation of 20°), while at the end plate the connections for rods 2 and 3 are paired together. The same pattern follows for the other pairs of wires. Rods 3 and 4, and 5 and 6 are paired at the base plate, while 4 and 5, and 6 and 1 are paired at the distal end. In the neutral configuration shown in Figure 4 with all leg lengths equal,

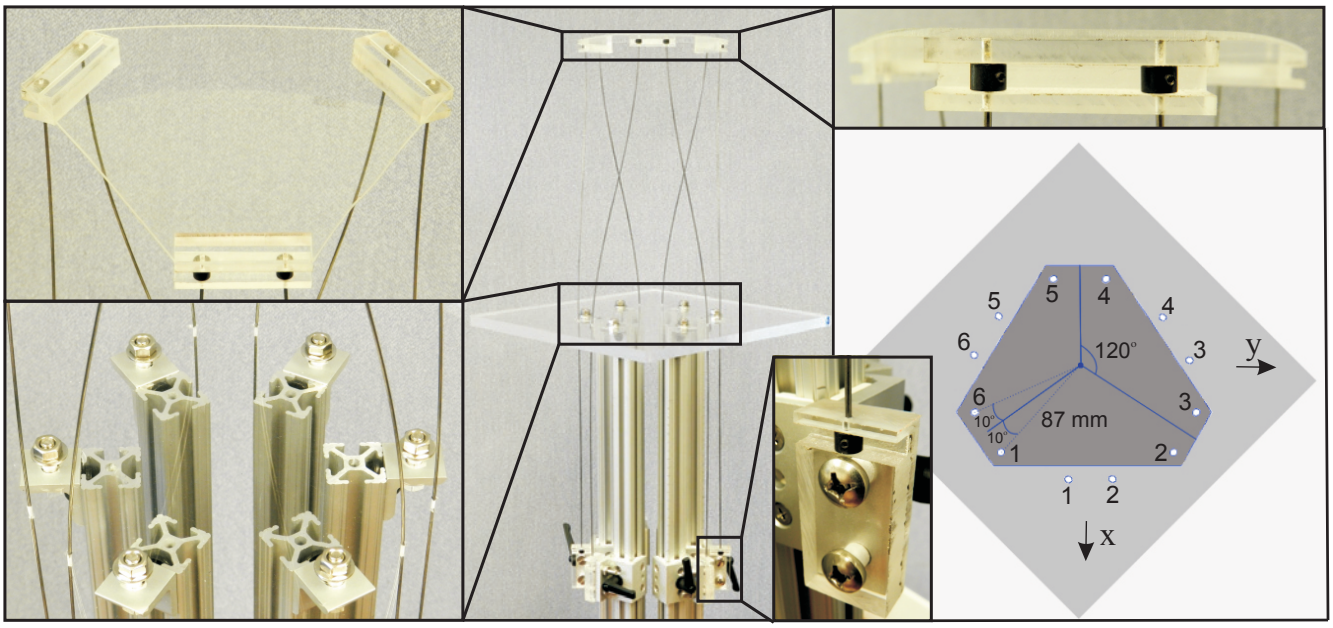

Fig. 3. The middle picture shows our prototype parallel continuum manipulator constructed for initial proof of concept and evaluation of our modeling approach. Close-up views of the base and end platforms are shown to the left. The dimensions and patterns of the base plate pass-through holes and the top platform connection points are detailed to the right. The lengths of the compliant legs between the two platforms are actuated by manually translating linear slides connected to the rod ends below the base platform.

this connection pattern causes the top plate to be rotated by 60° with respect to the hole pattern in the base plate and causes all of the rods to bend from their naturally straight state.

III. Modeling Approach

Building off of prior work on concentric-tube continuum robots [8] and tendon actuated continuum robots [4], we adopt a kinematic modeling approach for parallel continuum robots that is based on classical Cosserat rod mechanics [31]. The framework outlined in the following subsections addresses the forward and inverse kinematics and statics problems.

A. Cosserat Rod Equations

The shape of each component rod in the robot is defined by its position $\boldsymbol{p}_i(s_i) \in \mathbb{R}^3$ and material orientation $R_i(s_i) \in \mathrm{SO}(3)$, forming a material-attached reference frame $g_i(s_i) = \left[\begin{smallmatrix} R_i(s_i) & \boldsymbol{p}_i(s_i) \\ \mathbf{0} & 1 \end{smallmatrix}\right] \in \mathrm{SE}(3)$ as a function of arc length $s_i \in \mathbb{R}$ measured from the proximal platform. The position and orientation evolve along the length of the rod according to kinematic variables $\boldsymbol{v}_i(s) \in \mathbb{R}^3$ and $\boldsymbol{u}_i(s) \in \mathbb{R}^3$, which describe the linear and angular rates of change expressed in local or body frame coordinates of the material frame as follows:

$$\begin{aligned} \boldsymbol{p}_i' &= R_i \boldsymbol{v}_i, \\ R_i' &= R_i \widehat{\boldsymbol{u}}_i, \end{aligned} \tag{1}$$

where $'$ denotes a derivative with respect to s_i, and $\widehat{\ }$ denotes mapping from $\mathbb{R}^3$ to $\mathfrak{so}(3)$ as follows,

$$\widehat{\boldsymbol{a}} = \begin{bmatrix} 0 & -a_3 & a_2 \\ a_3 & 0 & -a_1 \\ -a_2 & a_1 & 0 \end{bmatrix}. \tag{2}$$

As in [32], we also use $\vee$ to denote the inverse mapping of $\widehat{\ }$, i.e. $(\widehat{\boldsymbol{u}})^\vee = \boldsymbol{u}$.

As derived in [4], [8], [31], the rates of change of the internal force vector $\boldsymbol{n}$ and internal moment vector $\boldsymbol{m}$ with respect to the arc length s_i are described by the classical Cosserat rod differential equations of static equilibrium:

$$\begin{aligned} \boldsymbol{n}_i' &= -\boldsymbol{f}_i \\ \boldsymbol{m}_i' &= -\boldsymbol{p}_i' \times \boldsymbol{n}_i - \boldsymbol{l}_i, \end{aligned} \tag{3}$$

where all vectors are assumed expressed in global coordinates, and $\boldsymbol{f}_i$ and $\boldsymbol{l}_i$ are distributed force and moment vectors respectively applied per unit length to rod i. Distributed self weight and any other external forces are straightforward to include within $\boldsymbol{f}_i$ and $\boldsymbol{l}_i$.

The kinematic variables $\boldsymbol{v}_i$ and $\boldsymbol{u}_i$ are related to material strain (shear, extension, bending, and torsion) and can be used to calculate the internal force and moment vectors (denoted by vectors $\boldsymbol{n}$ and $\boldsymbol{m}$ respectively and expressed in global coordinates) via a material constitutive law. For the present, we use a linear constitutive relationship of the following form,

$$\begin{aligned} \boldsymbol{n}_i &= R_i K_{se,i} \left(\boldsymbol{v}_i - \boldsymbol{v}_i^*\right), \quad K_{se,i} = \begin{bmatrix} A_i G_i & 0 & 0 \\ 0 & A_i G_i & 0 \\ 0 & 0 & A_i E_i \end{bmatrix} \\ \boldsymbol{m}_i &= R_i K_{bt,i} \left(\boldsymbol{u}_i - \boldsymbol{u}_i^*\right), \quad K_{bt,i} = \begin{bmatrix} E_i I_i & 0 & 0 \\ 0 & E_i I_i & 0 \\ 0 & 0 & J_i G_i \end{bmatrix} \end{aligned} \tag{4}$$

where $\boldsymbol{v}_i^*$ and $\boldsymbol{u}_i^*$ are the kinematic variables of the rod in an assigned stress free reference state. For an initially straight rod, appropriate reference state variables are $\boldsymbol{v}_i^* = [0\ 0\ 1]^T$ and $\boldsymbol{u}_i^* = [0\ 0\ 0]^T$. The matrices $K_{se,i}$ and $K_{bt,i}$ here contain the stiffness terms for a radially symmetric rod cross-section

which could vary with arc length, involving the area A_i, Young's modulus, E_i, the shear modulus G_i, the second area moment I_i (about the local x and y axes), and the polar area moment J_i about the local z axis.

Thus, for each rod, equations 1, 3, and 4 form a system of differential equations that describes the evolution of the state variables $\boldsymbol{p}_i$, R_i, $\boldsymbol{m}_i$, and $\boldsymbol{n}_i$ with respect to s_i.

B. Boundary Conditions for Forward Kinematics

Each rod or tube in a parallel continuum robot is independently described by the system of differential equations above. However, the boundary conditions of each system are coupled because of the physical constraints inherent to the robot structure.

For the prototype robot design which we describe in Section II, the proximal end of each rod is clamped with a set-screw shaft collar constrained within a groove in acrylic block, and each rod subsequently passes through a cylindrical hole in the base platform as shown in Figure 3. This design constrains the position $\boldsymbol{p}_i$ and the rod tangent vector at the base platform while allowing rotational freedom about the tangent axis so that no torsional moment can be supported. Thus, we set the torsional moment to zero at the base of each rod and express $R_i(0)$ as a rotation about the global z-axis by some angle θ_i as follows:

$$\begin{aligned} m_{iz}(0) &= 0 \\ R_i(0) &= \begin{bmatrix} \cos\theta_i & -\sin\theta_i & 0 \\ \sin\theta_i & \cos\theta_i & 0 \\ 0 & 0 & 1 \end{bmatrix} \end{aligned} \tag{5}$$

At the distal end of each rod ($s_i = L_i$), the following conditions of static equilibrium must hold for the top plate:

$$\begin{aligned} &\sum_{i=1}^{n} [\boldsymbol{n}_i(L_i)] - \boldsymbol{F} = \boldsymbol{0} \\ &\sum_{i=1}^{n} [\boldsymbol{p}_i(L_i) \times \boldsymbol{n}_i(L_i) + \boldsymbol{m}_i(L_i)] - \boldsymbol{p}_c \times \boldsymbol{F} - \boldsymbol{M} = \boldsymbol{0}, \end{aligned} \tag{6}$$

where $\boldsymbol{F}$ and $\boldsymbol{M}$ are external force and moment vectors applied at the centroid of the top plate, $\boldsymbol{p}_c$. The clamped connections of the distal end of the rods to the top plate are modeled by setting the material orientations of each rod at L_i equal to each other:

$$\left[\log\left(R_i^T(L_i) R_1(L_1)\right)\right]^{\vee} = \boldsymbol{0} \text{ for } i = 2...n, \tag{7}$$

where $\log()$ is the matrix natural logarithm, which maps $\mathrm{SO}(3)$ to $\mathfrak{so}(3)$, and the $\vee$ operator subsequently maps $\mathfrak{so}(3)$ to $\mathbb{R}^3$. This forces a common material orientation for all the distal rod ends.

Finally, we can write the following equations for the rod end positions.

$$\boldsymbol{p}_1(L_1) - \boldsymbol{p}_i(L_i) - R_1(L_1)\left(\boldsymbol{r}_1 - \boldsymbol{r}_i\right) = \boldsymbol{0} \text{ for } i = 2...n, \tag{8}$$

where $\boldsymbol{r}_i$ is the connection position for rod i expressed with respect to the top plate coordinate system. These are analogous to loop closure equations because they are only satisfied when the positions of the rod ends have the same relative positions as the connection pattern in the top plate.

C. Boundary Conditions for Inverse Kinematics

For the inverse kinematics problem, the boundary conditions given above in (5) and (6) still apply, but the geometric coupling of the rods at the distal platform is simplified by the fact that a desired position and orientation is known. This can be expressed by a constraint on the position and orientation of each distal leg end as follows:

$$\begin{aligned} \left[\log\left(R_i^T(L_i) R_d\right)\right]^{\vee} &= \boldsymbol{0} \text{ for } i = 1...n, \\ \boldsymbol{p}_d + R_d \boldsymbol{r}_i - \boldsymbol{p}_i &= \boldsymbol{0} \text{ for } i = 1...n. \end{aligned} \tag{9}$$

where $\boldsymbol{p}_d$ and R_d are the desired position (of the centroid) and orientation of the distal platform. We note that these equations are applied for $i = 1...n$, so there are a total of six more scalar constraint equations to be solved than in the forward kinematics case, and the leg lengths constitute n additional unknowns.

D. Numerical Computation

A simple shooting method provides an effective way to solve the systems of rod equations subject to these coupled boundary conditions. In this procedure, the unknown boundary conditions at the base of each rod ($\boldsymbol{n}_i(0)$, $m_{ix}(0)$, $m_{iy}(0)$, and θ_i) are guessed (in the inverse kinematics case, the leg lengths L_i are included in this set of unknowns). Each system of rod equations is numerically integrated from $s_i = 0$ to L_i as an initial value problem using a standard numerical routine such as a Runge-Kutta method, and the boundary condition equations are subsequently evaluated. This process is nested within an optimization loop which iteratively updates the guessed values for the unknown proximal boundary conditions until the distal boundary conditions are satisfied within an appropriate tolerance. We have found this to be an efficient and relatively stable method of computation. For the examples shown in the experimental section, convergence was achieved in every case, starting with an uninformed initial guess of zero for all unknown proximal conditions. Computation time was on the order of 10 seconds using unoptimized MATLAB code executed on a typical laptop computer. Computation time decreases to about 1 second if a good initial guess is available, which enables simulation of quasistatic motion since a previous solution can be used as the initial guess for the next iteration.

E. Multiple Solutions and Buckling Behavior

In contrast to rigid-link robots, the forward and inverse kinematics problems for parallel continuum manipulators are *both* complex (with the potential for multiple solutions possible) due to the large-deflection elastic behavior involved. For our numerical computation strategy above, the set of values for the unknown initial conditions (and leg lengths in the case of inverse kinematics) which satisfies the distal end boundary conditions may not always be unique. In this context, the phenomena of "buckling" describes the sudden transition of one valid solution to another one,

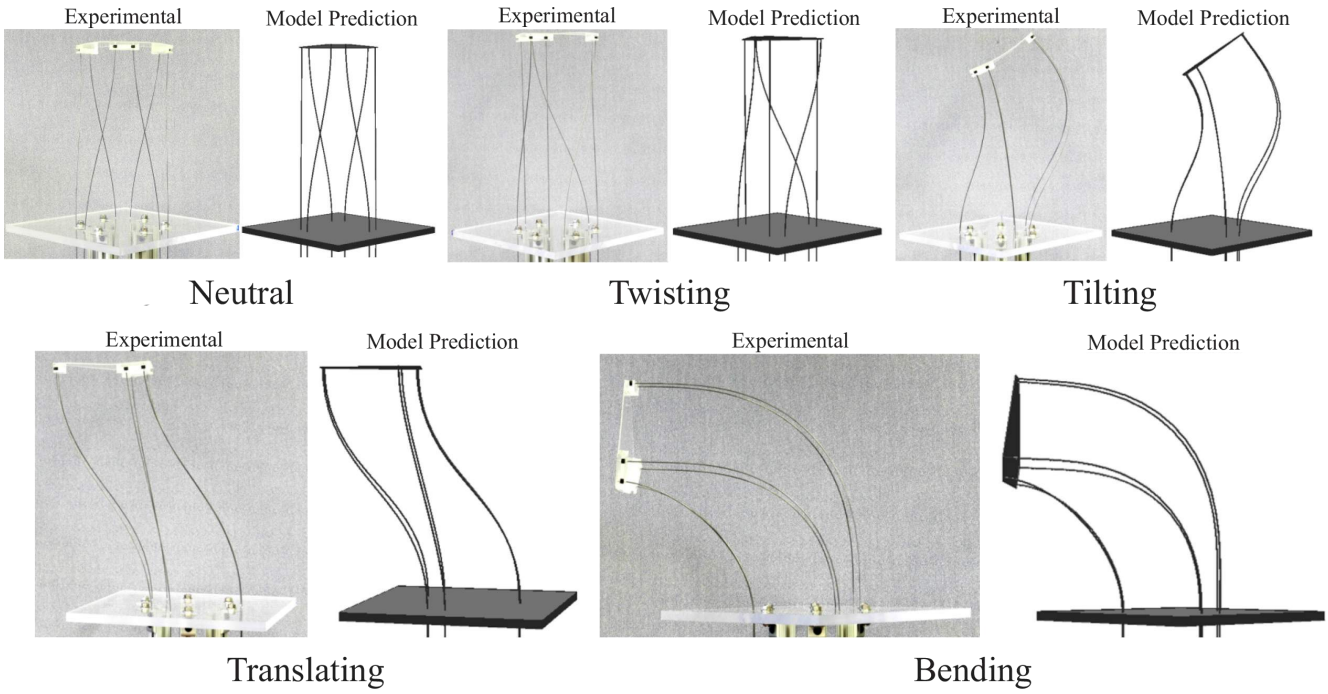

Fig. 4. We show photographs of five experimental configurations, demonstrating the ability of our prototype parallel continuum manipulator to execute axial twist, transverse tilt, translation, and bending (simultaneous translation and tilt). To the right of each experimental photograph, we show a MATLAB rendering of our rod-mechanics-based kinematic model prediction for the same actuator configurations.

which may occur when a particular equilibrium solution becomes unstable (or ceases to exist) as the result of a small change in actuation or external loading. The model equations are still valid in these situations, and they contain the ability to accurately describe all possible "buckled" states if the correct solution for the initial conditions is selected. The quasistatic simulation process described above tends to produce the correct solution until a point of instability is reached. The potential for buckling and instability exists for all continuum robots when external loads are considered, and for some designs even without external loading (e.g. concentric-tube robots). Snap-through instabilities have been studied for particular continuum robots [33], [34], but further work is needed to address methods for detecting and avoiding potential buckling in continuum robots.

IV. Kinematic Simulation and Analysis

Figure 4 demonstrates the kinematic degrees of freedom and range of motion of our prototype manipulator structure by showing the manipulator shape in five different configurations. With all leg lengths equal, the robot is in a straight, neutral state, which can be raised or lowered by equal translation of the legs. By extending legs 2, 4, and 6, the distal platform twists about the z-axis. Translating legs 4 and 5 causes the platform to tilt, and translating legs 3 and 6 causes translation. A combination of rotation and translation (bending) is achieved by extending legs 4 and 5 while retracting legs 1 and 2. The collection of legs maintains a compact form throughout all these motions, which is encouraging for potential applications in confined spaces. Figure 4 also shows a rendering of our forward kinematics model solution for these five cases, indicating the feasibility and qualitative accuracy of the modeling approach over a wide range of motion. We provide further quantitative assessment of model accuracy in Section V.

To further illustrate the kinematics of the prototype design, we give the body-frame manipulator Jacobian, J^b as defined in [32], which we computed numerically for the prototype manipulator in the neutral configuration (where all leg lengths are 406 mm, and the rotation is aligned with the global reference frame.),

$$J^b = \begin{bmatrix} -1.62 & -1.62 & 1.83 & -0.21 & -0.21 & 1.83 \\ -1.18 & 1.18 & -0.82 & -2.00 & 2.00 & 0.82 \\ 0.17 & 0.17 & 0.17 & 0.17 & 0.17 & 0.17 \\ -0.12 & 0.12 & 0.24 & 0.12 & -0.12 & -0.24 \\ -0.20 & -0.20 & 0.00 & 0.20 & 0.20 & 0.00 \\ -0.65 & 0.65 & -0.65 & 0.65 & -0.65 & 0.65 \end{bmatrix},$$

where the top 3 rows are dimensionless, and the bottom three rows have units of degrees/mm. The matrix is full rank and well conditioned, indicating that in the neutral configuration, actuators can easily move the top platform in any direction in the 6 DOF space of rigid body motion.

In Figure 5, we depict the inverse kinematic mapping over 3 two-dimensional slices of the workspace. The figure shows the required leg length and axial tension at the base of each leg as a function of the desired end-effector pose, which is specified by position $\boldsymbol{p}_d = [x\ y\ z]^T$ and orientation $R_d = \exp(\widehat{\boldsymbol{\theta}})$, $\boldsymbol{\theta} = [\theta_x\ \theta_y\ \theta_z]^T$. For each slice, two of the six pose variables were varied over a 9x9 grid of values for which the inverse kinematics computation easily converged, while all other pose variables were held constant at their nominal values of $x = y = \theta_x = \theta_y = \theta_z = 0$, and $z = 400$ mm.

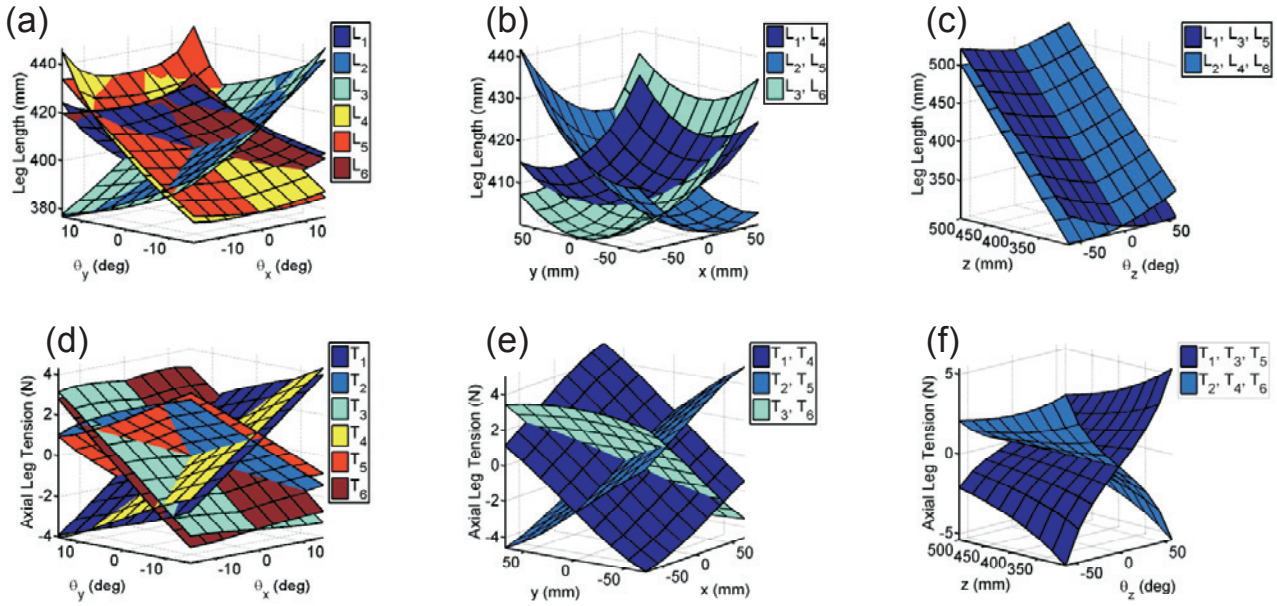

Fig. 5. By solving the inverse kinematics formulation of the model equations in Section III, we explore three two-dimensional slices of the workspace for our prototype design described in Section II, centered about a nominal workspace point $\boldsymbol{p}_d = [0 \;\; 0 \;\; 400 \text{ mm}]^T$, $R_d = I$. (a) and (d): The required leg lengths (a) and axial tension at the base of each leg (d) are plotted as a function of desired angular displacements of the distal platform about the global x and y axes while holding the desired position constant. (b) and (e): The required leg lengths (b) and axial tension at the base of each leg (e) are plotted as a function of desired displacements in the global x and y directions while holding the desired orientation constant. (c) and (f): The required leg lengths (c) and axial tension at the base of each leg (f) are plotted as a function of desired displacement along and rotation about the global z axis while holding all other pose variables constant.

The first case (Figure 5: (a) and (d)) shows an approximately linear kinematic mapping for desired rotation about the x and y axes. The second case (Figure 5: (b) and (e)) shows an approximately quadratic leg length mapping and an approximately linear tension mapping for desired translation in the $x-y$ plane. We note that in this case, the required lengths and tensions are identical for legs 1 and 4, 2 and 5, and 3 and 6 respectively. The final case (Figure 5: (c) and (f)) shows an approximately linear leg length mapping and an approximately cubic tension mapping for desired motion which both rotates about and translates along the global z axis. In this case, the lengths and tensions are identical for legs 1, 3, and 5, and 2, 4, and 6 respectively.

The axial tension at the base of each leg corresponds to the actuator force which would be required to hold the robot in a particular configuration. We conclude that over these ranges of motion, moderate forces on the order of 5 N will be required to actuate the structure. A simulation of this kind can be used in the design process to size motors for a particular set of manipulator structural parameters, and to limit the length that the legs extend below the base platform to avoid buckling.

We can also compute the output stiffness matrix at the top platform, which maps displacement of the end effector centroid to applied force $d\boldsymbol{F} = Kd\boldsymbol{p_c}$. For the neutral configuration in Figure 4, the computed stiffness matrix is

$$K = \begin{bmatrix} 17 & 0 & 0 \\ 0 & 17 & 0 \\ 0 & 0 & 122 \end{bmatrix} N/mm,$$

while for the bending configuration in Figure 4, the stiffness matrix is computed to be

$$K = \begin{bmatrix} 12.7 & 0 & 12.8 \\ 0 & 0.5 & 0 \\ 12.8 & 0 & 14.5 \end{bmatrix} N/mm.$$

These computations show that the stiffness in the y direction (out of the page for the bending case in Figure 4), is only about 3% of its value in the straight case, which is consistent with our experience with this prototype. We conclude that care should be taken when designing and controlling a parallel continuum manipulator to ensure that output stiffness is sufficient for the desired tasks.

V. Experimental Validation

We performed a set of model validation experiments by photographing the shape of our prototype manipulator in front of a graph poster in 14 different actuator configurations, which are listed in Table I. Figure 6 shows the basic elements of each image that were measured, the top platform centroid and orientation in the global $x-z$ plane. These measurements were then compared to our forward kinematics model prediction for each actuator configuration. The photos of these planar cases were taken perpendicular to the graph plane approximately 30 feet away from the robot so that perspective error was minimized.

The resulting differences between the data and the model prediction are presented in Table I. The positional error was calculated as the total Cartesian error in the global $x-z$ plane, and the percent error was calculated as the position error divided by the average leg length for each case. The maximum positional error was 11.74 mm with a 2.89%

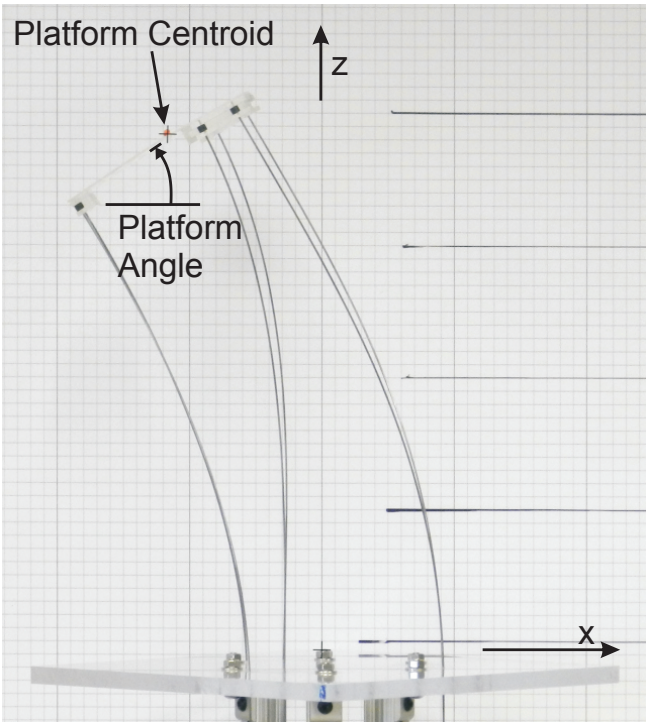

Fig. 6. The three main measurements taken from the images are the position of the centroid of the end effector plate in the x and z, which is denoted by the marker at the top, and the orientation of the end effector in the $x-z$ plane. The orientation was measured by drawing a line along the end effector edge and then measuring the slope of the line with the grid poster.

TABLE I

EXPERIMENTAL CONFIGURATIONS AND MODEL ERROR (MM)

#	L_1	L_2	L_3	L_4	L_5	L_6	Error	% Error
1	406	406	406	406	406	406	3.4	0.8
2	386	406	386	406	386	406	6.1	1.6
3	426	406	426	406	426	406	2.9	0.7
4	406	406	426	406	406	426	8.8	2.1
5	406	406	386	406	406	386	7.1	1.8
6	406	406	366	406	406	366	5.4	1.4
7	406	406	406	386	386	406	7.5	1.8
8	406	406	406	366	366	406	10.4	2.7
9	406	406	406	426	426	406	8.9	2.1
10	406	406	406	446	446	406	7.6	1.8
11	426	426	406	386	386	406	7.0	1.7
12	446	446	406	366	366	406	10.4	2.6
13	386	386	406	426	426	406	9.3	2.3
14	366	366	406	446	446	406	11.7	2.9

associated percent error. For the configurations resulting in a change in top platform orientation (7-14 in Table I), angular displacement was measured graphically as shown in Figure 6, and the maximum angular difference between model prediction and experiment was 3.14 degrees.

We observed a small amount of flex in the top acrylic plate during the experiments. This unmodeled effect is a source of error between model prediction and actual manipulator shape. Future designs should mitigate this inaccuracy by designing the top plate thickness to better handle the expected

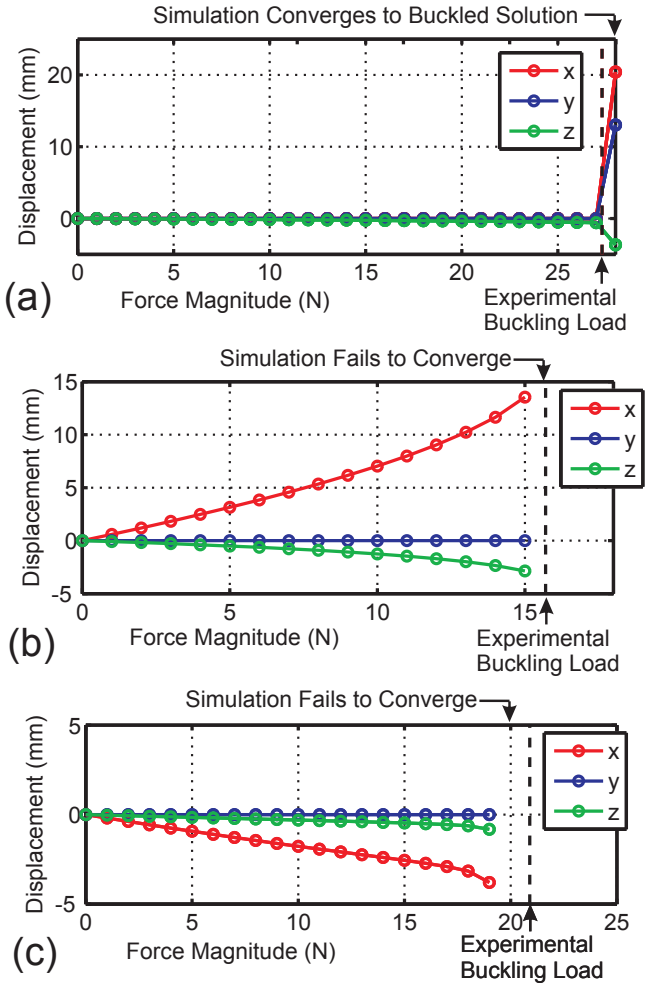

Fig. 7. Displacements of the top platform centroid in the x, y, and z directions are plotted by using our forward kinematics model to perform quasistatic simulation with an incrementally increasing vertical load for three different manipulator configurations (1, 4, and 5 in Table I) . The black dashed lines depict the experimentally determined critical buckling loads for the same cases. (a) The simulation converged to a buckled solution at an applied load very close to the experimentally determined buckling load. (b) and (c) The simulation failed to converge to any solution just prior to when the simulated load would have reached the experimentally determined buckling load.

reaction moments which can be determined using the model.

A. Buckling Experiments

We also experimentally determined a critical buckling load for the prototype structure in three different actuator configurations, (1, 4, and 5 in Table I, corresponding to a straight neutral case and two translating cases, respectively). We applied an incrementally increasing force in the negative z direction (down) through the centroid of the top plate until at least one leg in the structure began to buckle. The resulting experimental buckling loads are shown by the black dashed lines in Figure 7. When running a forward kinematics model simulation with the same incrementally increasing force, our simulation converged to a buckled solution (shown

by the sudden large centroid displacement in Figure 7 (a)) at a load close to the experimentally determined buckling load. For configurations 4 and 5 ((b) and (c) in Figure 7), the simulation failed to converge to a valid forward kinematics solution just prior to reaching the experimentally determined buckling load, indicating that the buckled mode is not relatively close to the unbuckled state.

VI. Conclusions

We have provided several new results toward a general understanding of design and kinematics for parallel continuum manipulators. The Cosserat-rod modeling approach shows good agreement with the data from our experiments, and our kinematic analysis demonstrates the feasibility of achieving 6 DOF dexterity and a large range of motion with a design similar to a rigid-link Stewart-Gough platform, although output stiffness can vary widely over the workspace. Future design work is needed to quantify tradeoffs and scaling laws, address miniaturization and actuation for endoscopic surgical applications, and integrate mechatronic control systems. On the theoretical side, dynamics models are needed, and a rigorous treatment of buckling is necessary in order to restrict designs and/or operating regions for safety.

References

[1] R. J. Webster, III and B. A. Jones, "Design and Kinematic Modeling of Constant Curvature Continuum Robots: A Review," *The International Journal of Robotics Research*, vol. 29, no. 13, pp. 1661–1683, 2010.

[2] W. McMahan, V. Chitrakaran, M. M. Csencsits, D. Dawson, I. D. Walker, B. A. Jones, M. Pritts, D. Dienno, M. Grissom, and C. D. Rahn, "Field trials and testing of the OctArm continuum manipulator," *IEEE International Conference on Robotics and Automation*, pp. 2336–2341, 2006.

[3] J. Ding, R. E. Goldman, K. Xu, P. K. Allen, D. L. Fowler, and N. Simaan, "Design and Coordination Kinematics of an Insertable Robotic Effectors Platform for Single-Port Access Surgery," *IEEE/ASME Tr*, vol. 18(5), pp. 1612–1624, 2013.

[4] D. C. Rucker and R. J. Webster III, "Statics and Dynamics of Continuum Robots With General Tendon Routing and External Loading," *IEEE Transactions on Robotics*, vol. 27, no. 6, pp. 1033–1044, Dec. 2011.

[5] D. B. Camarillo, C. F. Milne, C. R. Carlson, M. R. Zinn, and J. K. Salisbury, "Mechanics Modeling of Tendon-Driven Continuum Manipulators," *IEEE Transactions on Robotics*, vol. 24, no. 6, pp. 1262–1273, 2008.

[6] I. A. Gravagne, C. D. Rahn, and I. D. Walker, "Large-Deflection Dynamics and Control for Planar Continuum Robots," *IEEE/ASME Transactions on Mechatronics*, vol. 8, no. 2, pp. 299–307, Jun. 2003.

[7] P. E. Dupont, J. Lock, B. Itkowitz, and E. Butler., "Design and Control of Concentric-Tube Robots," *IEEE Transactions on Robotics*, vol. 26, pp. 209–225, 2010.

[8] D. C. Rucker, B. A. Jones, and R. J. Webster III, "A Geometrically Exact Model for Externally Loaded Concentric-Tube Continuum Robots," *IEEE Transactions on Robotics*, vol. 26, pp. 769–780, 2010.

[9] N. Simaan, R. Taylor, and P. Flint, "A Dexterous System for Laryngeal Surgery," *IEEE International Conference on Robotics and Automation*, pp. 351–357, 2004.

[10] No Title. [Online]. Available: http://www.festo.com/net/SupportPortal/Files/46268

[11] J.-P.Merlet, *Parallel Robots*, ser. Solid Mechanics and its Applications, G. M. L. Gladwell, Ed. Springer, 2006, vol. 128.

[12] X. Zhang, J. K. Mills, and W. L. Cleghorn, "Dynamic Modeling and Experimental Validation of a 3-PRR Parallel Manipulator with Flexible Intermediate Links," *Journal of Intelligent and Robotic Systems*, vol. 50, no. 4, pp. 323–340, Jul. 2007.

[13] B. Kang, B. Yeung, and J. K. Mills, "Two-time scale controller design for a high speed planar parallel manipulator with structural flexibility," *Robotica*, vol. 20, no. 05, pp. 519–528, Sep. 2002.

[14] G. Piras, W. Cleghorn, and J. Mills, "Dynamic finite-element analysis of a planar high-speed, high-precision parallel manipulator with flexible links," *Mechanism and Machine Theory*, vol. 40, no. 7, pp. 849–862, Jul. 2005.

[15] S. Briot and W. Khalil, "Recursive symbolic calculation of the dynamic model of flexible parallel robots," *IEEE International Conference on Robotics and Automation*, pp. 5433–5438, May 2013.

[16] S. Tzafestas, M. Kotsis, and T. Pimenides, "Observer-Based Optimal Control of Flexible Stewart Parallel Robots," *Journal of Intelligent and Robotic Systems*, vol. 34, no. 4, pp. 489–503, Aug. 2002.

[17] J. Lee and Z. Geng, "A dynamic model of a flexible stewart platform," *Computers & Structures*, vol. 48, no. 3, pp. 367–374, Aug. 1993.

[18] J. McInroy, "Modeling and design of flexure jointed Stewart platforms for control purposes," *IEEE/ASME Transactions on Mechatronics*, vol. 7, no. 1, pp. 95–99, Mar. 2002.

[19] W. Dong, L. Sun, and Z. Du, "Design of a precision compliant parallel positioner driven by dual piezoelectric actuators," *Sensors and Actuators A: Physical*, vol. 135, no. 1, pp. 250–256, Mar. 2007.

[20] J. Hesselbach and A. Raatz, "Compliant parallel robot with 6 DOF," in *Intelligent Systems and Advanced Manufacturing*, B. J. Nelson and J.-M. Breguet, Eds. International Society for Optics and Photonics, Oct. 2001, pp. 143–150.

[21] Y. Yun and Y. Li, "Design and analysis of a novel 6-DOF redundant actuated parallel robot with compliant hinges for high precision positioning," *Nonlinear Dynamics*, vol. 61, no. 4, pp. 829–845, Mar. 2010.

[22] O. Company, S. Krut, and F. Pierrot, "Analysis of a High Resolution Planar PKM," *12th IFToMM world Congress*, pp. 1–6, 2007.

[23] M. Goldfarb and J. Speich, "Eliminating non-smooth nonlinearities with compliant manipulator design," in *Proceedings of the 1998 American Control Conference. ACC (IEEE Cat. No.98CH36207)*, vol. 4. American Autom. Control Council, 1998, pp. 2118–2122.

[24] Y. Li and Q. Xu, "A Novel Design and Analysis of a 2-DOF Compliant Parallel Micromanipulator for Nanomanipulation," *IEEE Transactions on Automation Science and Engineering*, vol. 3, no. 3, pp. 248–254, 2006.

[25] M. L. Culpepper and G. Anderson, "Design of a low-cost nano-manipulator which utilizes a monolithic, spatial compliant mechanism," *Precision Engineering*, vol. 28, no. 4, pp. 469–482, 2004.

[26] C. Quennouelle and C. Gosselin, "Kinematostatic modeling of compliant parallel mechanisms," *Meccanica*, vol. 46, no. 1, pp. 155–169, Jan. 2011.

[27] F. Sergi, M. M. Lee, and M. K. OMalley, "Design of a series elastic actuator for a compliant parallel wrist rehabilitation robot," *IEEE International Conference on Rehabilitation Robotics*, 2013.

[28] C. Amici, A. Borboni, R. Faglia, D. Fausti, and P. Magnani, "A parallel compliant meso-manipulator for finger rehabilitation treatments: Kinematic and dynamic analysis." *2008 IEEE/RSJ International Conference on Intelligent Robots and Systems*, pp. 735–740, Sep. 2008.

[29] J. Peirs, D. Reynaerts, and H. V. Brussel, "Design of miniature parallel manipulators for integration in a self-propelling endoscope," *Sensors and Actuators*, vol. 85, pp. 409–417, 2000.

[30] Z. Zhu, H. Cui, and K. Pochiraju, "US 2008/0257096 A1. Flexible Parallel Manipulator for Nano-, Meso, or Macro-Positioning with Multi-Degrees of Freedom," 2008.

[31] S. S. Antman, *Nonlinear Problems of Elasticity*, 2nd ed., S. S. Antman, J. E. Marsden, and L. Sirovich, Eds. Springer Science, 2005.

[32] R. M. Murray, Z. Li, and S. S. Sastry, *A Mathematical Introduction to Robotic Manipulation*. Boca Raton, FL: CRC Press, 1994.

[33] R. J. Webster III, J. M. Romano, and N. J. Cowan, "Mechanics of Precurved-Tube Continuum Robots," *IEEE Transactions on Robotics*, vol. 25, no. 1, pp. 67–78, 2009.

[34] H. Mochiyama, A. Kinoshita, and R. Takasu, "Impulse Force Generator based on Snap-through Buckling of Robotic Closed Elastica : Analysis by Quasi-static Shape Transition Simulation," *IEEE/RSJ Int. Conf. on Intelligent Robots and Systems*, pp. 4583–4589, 2013.